Recombination of Hot Ionized Nebulae: The Old Planetary Nebula around V4334 Sgr (Sakurai's Star)* [*] This investigation makes use of

(article starts on next page)

Recombination of Hot Ionized Nebulae: The Old Planetary Nebula around V4334 Sgr (Sakurai's Star)[*]

Martin Reichel[1] , Stefan Kimeswenger[1,2] , Peter A. M. van Hoof[3] , Albert A. Zijlstra[4] , Daniela Barría[5] ,
Marcin Hajduk[6] , Griet C. Van de Steene[3] , and Daniel Tafoya[7]

[1] Institut für Astro- und Teilchenphysik, Universität Innsbruck, Technikerstr. 258, 6020 Innsbruck, Austria; Stefan.Kimeswenger@uibk.ac.at
[2] Instituto de Astronomía, Universidad Católica del Norte, Av. Angamos 0610, Antofagasta, Chile
[3] Royal Observatory of Belgium, Ringlaan 3, B-1180 Brussels, Belgium
[4] Jodrell Bank Centre for Astrophysics, Alan Turing Building, University of Manchester, Manchester, M13 9PL, UK
[5] Facultad de Ingeniería y Arquitectura, Universidad Central de Chile, Av. Francisco de Aguirre 0405, La Serena, Coquimbo, Chile
[6] Space Radio-Diagnostics Research Centre, University of Warmia and Mazury, Prawocheńskiego 9, 10-720 Olsztyn, Poland
[7] Department of Space, Earth and Environment, Chalmers University of Technology, Onsala Space Observatory, SE-439 92 Onsala, Sweden

Abstract

After becoming ionized, low-density astrophysical plasmas will begin a process of slow recombination. Models for this still have significant uncertainties. Recombination cannot normally be observed in isolation, because the ionization follows the evolutionary timescale of the ionizing source. Laboratory experiments are unable to reach the appropriate conditions because of the very long required timescales. The extended nebula around the very late helium pulse (VLTP) star V4334 Sgr provides a unique laboratory for this kind of study. The sudden loss of the ionizing UV radiation after the VLTP event has allowed the nebula to recombine free from other influences. More than 290 long-slit spectra taken with FORS1/2 at ESO's Very Large Telescope between 2007 and 2022 are used to follow the time evolution of the lines of H, He, N, S, O, and Ar. Hydrogen and helium lines, representing most of the ionized mass, do not show significant changes. A small increase is seen in [N II] ($+2.8\%$ yr^{-1}; 2.7σ significance), while we see a decrease in [O III] (-1.96% yr^{-1}; 2.0σ significance). The [S II] lines show a change of $+3.0\%$ yr^{-1} (1.6σ significance). The lines of [S III] and of [Ar III] show no significant changes. For [S III], the measurement differs from the predicted decrease by 4.5σ. A possible explanation is that the fractions of S^{3+} and higher are larger than expected. Such an effect could provide a potential solution for the sulfur anomaly in planetary nebulae.

1. Introduction

When UV radiation that photoionizes a nebula ceases, the ions begin to recombine. This is an important process in photoionized nebulae with typical densities of a few tens to a few hundred particles per cubic centimeter, where the slow recombination leaves the nebula out of equilibrium. These conditions exist in low-density H II regions, in planetary nebulae (PNe) and in nebulae around post-common-envelope binaries of the BE UMa family. Recombination at these low densities is not well studied, neither in astrophysical environments nor in the laboratory.

Laboratory studies aim to measure these effects directly. But appropriate density and excitation conditions are difficult to reach. The leading edge experiment Cryogenic Storage Ring has recently reached particle densities down to 140 cm^{-3} (Kreckel et al. 2019). In order to keep the free flight time (avoiding wall interaction) larger than the ion lifetimes, temperatures of a few kelvin are used. This is suitable for simulating conditions of cold molecular clouds in the interstellar medium. However, these have very low ionization levels. Ionized nebulae have typical temperatures of $T_e \gtrsim 10,000$ K; at such temperatures, the mean free path of particles can reach thousands of kilometers, meaning chamber wall interactions would dominate laboratory experiments.

Astrophysical targets are needed for the determination of the recombination timescales under these conditions, and for the verification of theoretical models. While ionization happens on timescales of the light travel time through nebulae, and thus within weeks or months, recombination happens very slowly (Schönberner 2008; Balick et al. 2021). The latter authors estimate that the expected recombination rate of the monoatomic gas per ion is

$$R_{\rm rec} = 10^5 \ {\rm yr}/(Z^2 n_e), \tag{1}$$

where Z is the ionic charge and n_e is the electron density. These calculations are based on a monatomic gas in a two-level approximation (Osterbrock & Ferland 2006) and assume that the ion is in the ground state. The latter assumption holds only for H, He, and noble gases, where the first excitation level is at >10 eV and thus collisional excitation is not contributing at all. Once fluorescence and interactions between ionic species are taken into account, excitation may change some approximations (see the discussion in Section 3.2.5 in Ferland et al. 2017). The interactions between species are partly included in a

simplified model by Koskela et al. (2012) for elements up to oxygen. Ferland et al. (2017) discuss in the implementation of the full collisional-radiative mode of the H- and He-like isoelectronic sequences, where ionization out of highly excited states can alter the ionization balance in some density regimes. Whether this is an important issue in our targets remains an open question.

For most nebulae, the dominant astrophysical evolutionary timescale is that of their ionizing source. The source (star) may heat up very rapidly, but, as mentioned, the ionizing timescale is very short (Schönberner 2008). Cooling or dimming of the ionizing source, causing recombination, happens on timescales of thousands to hundreds of thousands of years in most targets of interest. An exception might be the PNe around massive progenitor stars. However, their nebulae are very dense and only in the very outskirts can weak effects be determined (e.g., NGC 6445; van Hoof et al. 2000).

Hence recombination evolution is dominated by the dimming/cooling timescale of the ionizing source. There are only a handful of exceptional targets, suffering fast cooling and/or dimming, where we in fact are able to investigate isolated recombination in situ without major obfuscation caused by other processes. Here we present an observational study of V4334 Sgr spanning a period of more than 16 years. It suffered from a very late thermal pulse (VLTP) which caused a sudden loss of ionizing UV radiation. This caused the onset of recombination in the old PN surrounding V4334 Sgr. Pollacco (2002) finds no discernible recombination through the first three years of evolution after the event, while Schönberner (2008) argues that the total timescale is dominated by the ionization timescale and that a new recombined equilibrium is reached after only a few months.

2. The Target

In 1996 Nakano et al. (1996) discovered rebrightening of Sakurai's Star (V4334 Sgr), a cool post-AGB star. It was surmised to have undergone a VLTP around 1991 or 1992 (Herwig 2001; Lawlor & MacDonald 2003; Hajduk et al. 2005; Miller Bertolami et al. 2006). The star was found to be at the center of an old PN. After the eruption, the star expelled a new shell, located inside the old, now recombining PN. Since then spectra have been taken frequently. These provide the first closely spaced time series of spectra of an ionized nebula that undergoes recombination without any reionization by UV photons emitted by the central star.

Evolutionary models predict reheating of the star of V4334 Sgr to temperatures that would result in renewed photoionization of the nebula (Hajduk et al. 2005), but they differ on the expected timescale for this. However, no evidence for a hot stellar continuum or stellar wind features have been found in optical or infrared spectra so far (Hinkle et al. 2020). No evidence for increasing free–free radio emission from the newly ejected matter has been found either (M. Hajduk et al., in preparation). Moreover, our FORS long-slit spectra show a very red continuum of the central source V4334 Sgr in the optical. During the first years of the campaign, the continuum of the central source was not detected. Later it slowly appeared above the detection limit. Stacking the spectra taken in 2017 leads us to an estimated $(B–V)$ of the continuum of about $+3\overset{m}{.}4$. If the central source had heated to something hotter than 10,000 K, the intrinsic colors $-0\overset{m}{.}3 \leqslant (B–V)_0 \leqslant 0\overset{m}{.}0$ (Ducati et al. 2001) would require optical

extinctions of $A_{\rm V} > 11\overset{m}{.}5$. This assumes that the observed continuum is generated by direct light. Scattering by circumstellar clouds, efficient in the the blue bands, leads, like the scattered-light residuals in R CrB stars, to an underestimate of the extinction (Clayton et al. 2011). The value fits well to the extinction derived by the photometric evolution when the shell was formed (Pavlenko & Duerbeck 2001). Similar results for the extinction were found by Koller & Kimeswenger (2001) for the older twin V605 Aql by comparing optical to infrared luminosities. This extreme extinction inhibits potential UV photons from the reheating central star from reaching the region of the old PN. Our Atacama Large Millimeter/submillimeter Array (ALMA) observations (Van de Steene et al. 2017; van Hoof et al. 2018) of HCN and HNC molecules in the newly ejected material give us an estimate of the UV flux in the core of 0.5 erg cm^{-2} s^{-1}, based on the recent investigation by Bublitz et al. (2022) in the clumps of the Helix nebula (NGC 7293). The molecular gas detected by ALMA is at most $0\overset{''}{.}3$ from the core (Hinkle et al. 2020). This gives an upper limit for the total UV flux in the compact core of $\leqslant 0.1\,L_\odot$. Moreover, this radiation will have a geometrical thinning of at least 1/500 before reaching the outer location of the old PN. Reionization of the old PN by UV photons from the post-VLTP star thus can currently be neglected for this study.

Other potential targets which could be used to study recombination have been discussed in the past. These include the late thermal pulse (LTP) stars FG Sge (Tylenda 1980; Arkhipova et al. 2009) and Hen 3-1357 (Stingray Nebula) (Reindl et al. 2017; Lawlor 2021; Balick et al. 2021), the VLTP star V605 Aql (studied by Lechner & Kimeswenger 2004; Koskela et al. 2012), and the very young dense PN SwSt 1 (Hajduk et al. 2020). Also, the nebulae around the family of post-common-envelope pre-cataclysmic BE UMa variables feature recombination effects (Mitrofanova et al. 2016; Kimeswenger et al. 2021 and references therein). However, all of those targets either do not have such a rapid evolution of the ionizing UV radiation, have much larger densities and thus very fast recombination in equilibrium, or are lacking an appropriate time coverage with homogeneous spectral data.

Thus our target provides a unique laboratory where the UV radiation was suddenly and completely switched off.

3. Data

The data sample used consists of a set of a few hundred long-slit spectra crossing the old PN nebula around the centraL VLTP object V4334 Sgr. These were obtained with the Very Large Telescope (VLT) unit telescopes (UTs) 1 and 2 using the FORS1/2 spectrographs (Appenzeller et al. 1998). The original purpose of the observations was to study the changes in the central star V4334 Sgr itself. Since the slit was always aligned in the same direction it is also possible to study the outer nebula as an unintended but perfectly homogeneous by-product. The entire project was conducted in service mode demanding good weather conditions (CLR). However, during the data reduction, some spectra with lower quality showed up. The data originally covered 11 observational epochs from 2007 to 2017 with 265 spectra. A few spectra were removed from this study, as the slit centering was not perfect in one run in 2011 (Reichel 2021). In 2022 (April 3 to 10) an additional set of 18 spectra were taken, improving the timeline which now spans over 16 observing seasons. The service mode logs always mention at least clear weather conditions and good seeing. However, after the additional calibration processing, we rejected 46 spectra due

Table 1
The GRISM Configurations That Were Used according to Anderson et al. (2017)

GRISM	Range (Å)	Resolution $\lambda/\Delta\lambda$	Dispersion (Å/pixel)	N
600V	4600–7096	990	0.74	23
600I	6790–8880	1500	0.66	12
600z	7466–10153	1260	0.81	3
300V	4610–8590	440	1.68	99
300I	6150–10190	660	1.62	100

Note. The usable wavelength range is given, ignoring the unused badly illuminated edges of the CCD. N gives the number of frames in the final sample with each grism.

Figure 1. The old PN around V4334 Sgr. Left: a single 300 s frame taken with the [O III] filter. Right: after star removal and averaging the two available frames (see the text). The black lines indicate the position of our slit. The old PN is $44''$ across.

to poor seeing or significant zero-point offsets. Thus a total sample of 237 spectra remained.

The VLT observations used five different low-resolution GRISMs[8] (Anderson et al. 2017; Reichel 2021). Table 1 provides an overview of the covered wavelength regime and the resolution near the central wavelength. There is some overlap between the spectra from the red and the blue setup which can be used as an additional test of the calibration quality and homogeneity of the data.

The data were taken between April and August of each year, with an east–west oriented slit. Two images, obtained from the ESO archive, were taken with FORS1 2002 October 2 using an [O III] narrowband filter. After each frame a second frame was taken using a filter for extragalactic observations redshifted by 6000 km s^{-1}. Those images were used to remove the stars. The slit position is indicated in Figure 1. A slit width of $1''0$ was used until 2016. In 2017 and 2022 a $1''3$ slit was used to cover the new ejecta of the VLTP which were growing in size. Further data were taken with FORS by other groups covering the time just after the outburst. However, as the slit position and orientation varied and mostly were far from our target position, they are not used here.

Observations were always conducted with the same sequence centered on an offset star in the direct images and blind offsetting to the faint target. Three spectra with exposure times around 900 s were taken. Such a sequence forms one observing block (OB). If another OB followed directly, the centering was redone to insure against pointing drifts or flexure. For each year and each GRISM two to four of these OBs were taken. The wavelength and basic flux calibrations were derived by the ESO FORS pipeline[9] (v5.6.2; Moehler et al. 2019) with the night sky removal deactivated to avoid partial removal of nebular lines. Then further manual steps were obtained in the framework of ESO MIDAS (Warmels 1992; Banse et al. 1983; European Southern Observatory 2013). These manual steps were (a) remove sky emission lines, (b) correct for sky transparency variations, (c) correct for seeing slit loss, and (d) manual extraction of the PN emission lines from the 2D spectra. Small MIDAS batch files were written to speed up and homogenize this interactive process. The four steps are described in detail below.
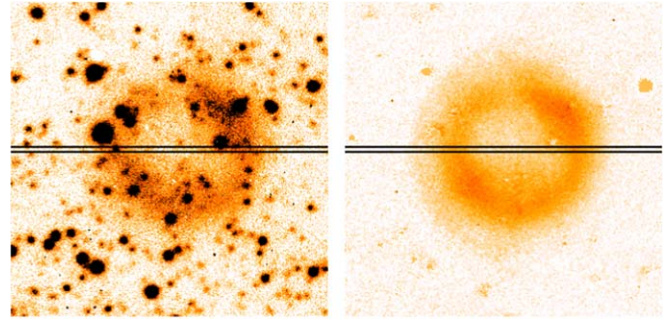
As the ESO pipeline is dedicated to stellar spectroscopy, the automated search for night sky emission lines also removes partially the lines of extended emission line objects like PNe. Thus this process was disabled in the pipeline. Moreover, along the $7'$ long slit some remnant of the optical curvature remains after the pipeline reduction. Star-free regions along the slit just outside the PN only about $20''$ from the nebula were used to derive a night sky emission line spectrum, which was used to subtract from the region of the PN in the 2D spectra.

The standard extinction curve derived by Patat et al. (2011) is automatically applied by the ESO pipeline. The typical airmass was between 1 and 1.1 (see Figure 2(a)). Thus the corrections were small. However as we had shown in observations of the scattered light at several nights near full moon, some offsets of transparency can occur even in very good nights (Jones et al. 2013, 2019). ESO standard stars, automatically used by the pipeline, are taken not very frequently during nights in the service mode calibration plan. Only a few of our OBs were taken at higher airmasses >1.35. Those where rejected from the final sample.

The flux zero points then were checked by the fluxes of field stars well centered in the slit. At the begin of an OB a slit preview image without the grism is taken for centering purposes. This was used to identify stars along the slit which are well centered. Solely those give a good calibration factor for the slit loss correction depending on the seeing only. Six stars (four on chip one, which also contains the optical center of the FOV, and thus the PN, and two on the second chip) were identified (Figure 3). Six frames from one night in 2011 with GRISM 300V were rejected as the sky region was taken erroneously with a few arcseconds offset. The ESO Ambient Conditions Database (ASM)[10] shows for the best photometric nights the zero points given by Patat et al. (2011). Those 26 spectra are used as the basis for the unity transparency 1.0. In fact, we measure later only relative variations with time. Therefore, the chosen absolute zero point is not of importance here. The median of the flux, integrated along the whole spectrum of the field stars, is used to define the offset. The scatter among them was of the order of 0^m05. Thus the differential error of the calibration of individual spectra should be of the order of $6^{-0.5} \times 0^m05 = 0^m02$. Figure 2(d) shows the distribution of the derived transparency values we used for corrections. They correspond well to the values of the ASM. We set a rejection limit at a transparency loss of -0^m25.

8　FORS VLT-MAN-ESO-13100-1543 Issue 101, 2017 August 24: http://www.eso.org/sci/facilities/paranal/instruments/fors/doc/VLT-MAN-ESO-13100-1543_P01.pdf.
9　VLT-MAN-ESO-19500-4106 v5.12, 2020 June: ftp.eso.org/pub/dfs/pipelines/instruments/fors/fors-pipeline-manual-5.12.pdf.

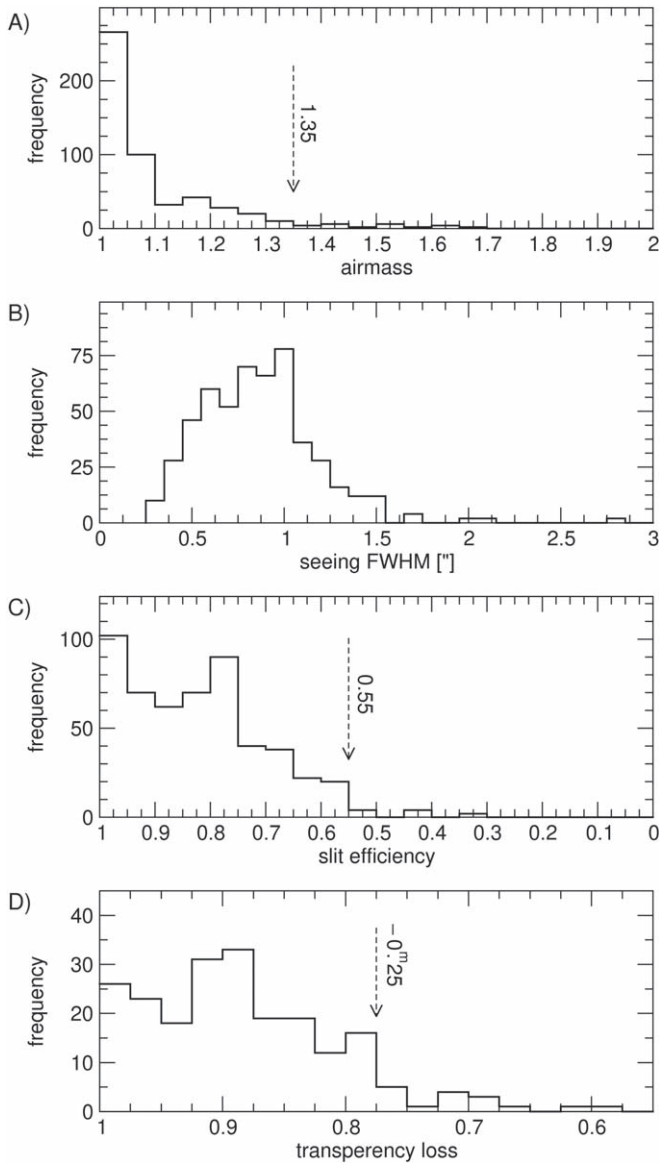10　http://archive.eso.org/cms/eso-data/ambient-conditions.html

Figure 2. Frequency distribution of the (a) airmass, (b) seeing, (c) slit efficiency calculated from the seeing, and (d) measured transparency losses. The arrows indicate the rejection limits applied for the sample (see the text).

The typical seeing was about $0\overset{''}{.}7$. However, seeing values up to $1\overset{''}{.}5$ sometimes occurred. A few spectra had extreme seeing and thus blurred images. The seeing was measured from the FWHM of the stellar images along the slit. The values corresponded well with those given by the ASM. Assuming Gaussian point spread functions (PSFs), the slit losses relative to the median FWHM were derived. ESO takes the standards for the service mode with very wide slits to be free of slit losses, but the pipeline does not apply a correction for the user's science frames. The flux calibration of a point source with a partially filled PSF in a slit and that of a homogeneous, slit-filling extended source differs. For this purpose, a small MIDAS batch was used to derive the factor of the filling by the calibration stars for each frame individually. The fraction of a 2D Gaussian with the derived FWHM was used to obtain the conversion factor (Figure 4). Generally, this was small as well as the slits were normally wider than the seeing. Figure 2 shows the distribution of the seeing values and the resulting slit efficiencies ($\equiv 1 -$ slit loss). A pair of direct consecutive nights

with seeings of $0\overset{''}{.}58$ and $1\overset{''}{.}13$ were used to estimate the errors of the correction procedure. They are in the order of $0\overset{m}{.}04$. The worst images with slit efficiencies below 0.55, which also are those showing blurry spectra, are rejected from the sample. At the PN lines, we assumed that the illuminations do not vary on the scale of the slit size. As the profiles along the slit also do not show very rapid flux variations we are confident that this assumption holds. A table containing all correction factors for the whole set of nearly 300 individual spectra can be found in the Appendix of Reichel (2021).

Finally the spectra of each PN line were extracted from the 2D spectra manually by marking interactively the line-emission region. Several field stars cross the region of the nebula (see Figures 1 and 6). Normally the stellar flux just beside the emission line is interpolated to correct for that. However, especially around the Balmer lines, the stellar flux under the nebular emission lines may behave differently than predicted by continuum interpolation for the star, due to strong Balmer absorption lines in the stellar spectra. As we are interested in variations only and not in the total PN flux, we masked these regions. Finally, the central region of V4334 Sgr was masked in order to exclude the recent ejecta (Hinkle & Joyce 2014; Hinkle et al. 2020), where the emission lines can be orders of magnitudes brighter than those of the PN (van Hoof et al. 2007, 2018). This avoids possible scattered light in the instrument (see Figure 5) arising from those lines of the VLTP core.

Within each set of three spectra of a single OB, the fluxes of the lines (integrated over the used area along the slit) do not vary beyond the photon noise. The same applies to the rare cases of OBs taken consecutively during the same night. However, between sets taken weeks to months apart, fluxes do vary slightly. As we do not expect physical processes to act in the PN on those timescales, we assume that these variations originate from weather and calibration inaccuracies. These variations give us a final estimate for the errors. For some lines, more than 20 individual measurements are available within some of years. All data points of one line for one GRISM within a year were averaged, giving the data point d_i and its standard deviation σ_i. In the case of independent data points, the error of a mean value is smaller than the standard deviation of the individual measurements. Then, our error would be smaller by a factor of 2 to 4. But we are dominated by systematic, and not statistical, errors. Therefore, this approach might be too optimistic. To use this standard deviation as the error for d_i is a very conservative accessment. The measurements in the overlap region from the visual to the infrared GRISMs are treated as independent data sets. The values used in the statistical analysis are given for each data set and each year in Table 2.

Sets taken at higher and lower resolution by the 300V/I and 600V/I GRISMs overlap in the region of the Hα line. Figure 6 shows the region of overlap and the various resolution effects. In case of the low-resolution GRISMs, the [N II] 6548 Å line slightly blends with H I 6563 Å. However, the nitrogen line originates from the same upper excitation level as [N II] 6584 Å. Thus the line ratio is fixed to a value of 2.96 by the ratio of the quantum mechanical transition strengths A_{ki} multiplied by the ratio of the line wavelengths, taken from the NIST atomic database (Tachiev & Froese Fischer 2001). This allows us to reconstruct the undisturbed hydrogen flux. The He I 6679 Å line was too weak to be used for a significant

slit preview:

spectrum:

atm. OH

P1(7.5) 8-4 9679Å
P2(6.5) 8-4 9669Å

P1(6.5) 8-4 9607Å
P2(5.5) 8-4 9621Å

P1(5.5) 8-4 9567Å
P2(4.5) 8-4 9552Å

P1(4.5) 8-4 9519Å

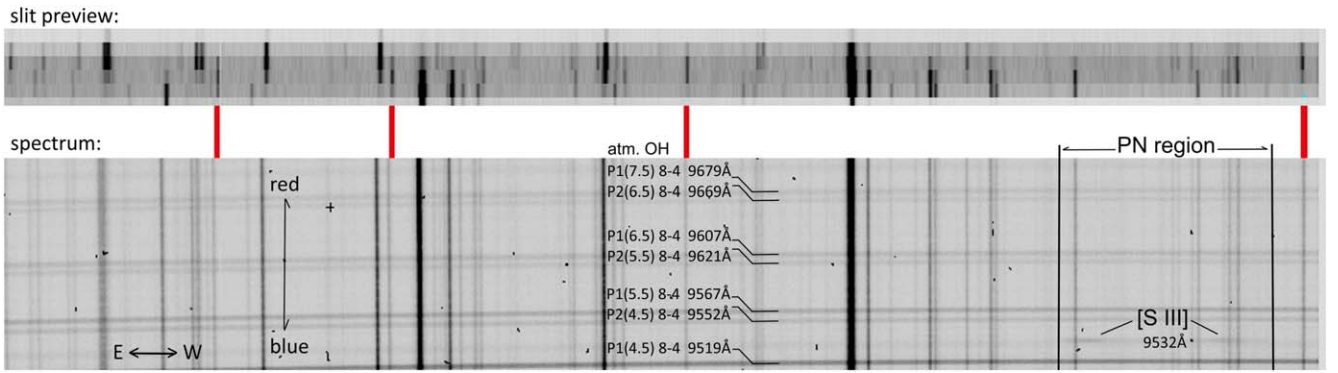PN region

[S III]
9532Å

red

E ⟷ W   blue

Figure 3. The selection of calibration stars. The upper panel shows a direct image taken through the slit (expanded in the *y*-direction to enhance the visibility of the centering) before adding the GRISM. Only well-centered stars were selected for calibration purposes. The lower panel shows a fraction of the red end of the spectrum taken directly thereafter. The selected calibration stars are marked with the red bars connecting their image in the slit preview with their appearance in the spectrum. The night sky line identifications are taken from Osterbrock et al. (1996).
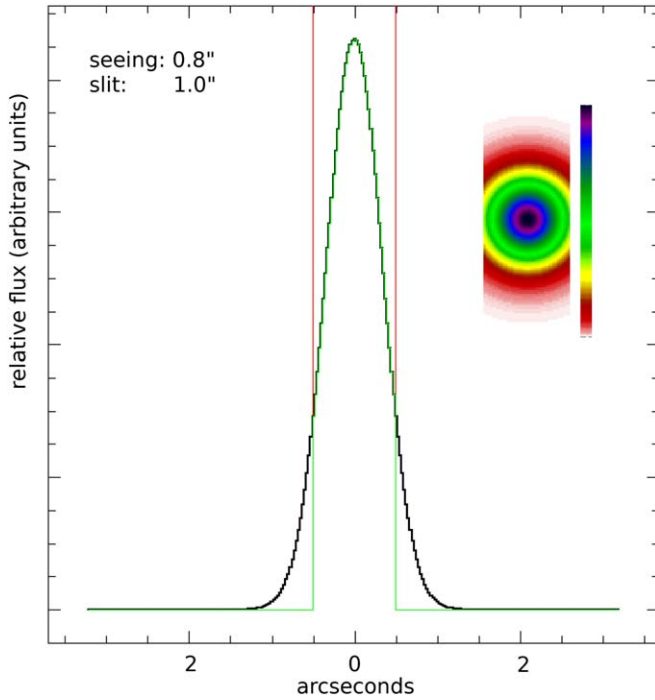

Figure 4. The slit loss calibration. A cut through the stellar image (black), the slit boundaries (red), and the resulting remaining flux reaching the instrument (green). The insert shows the full 2D representation on a linear color scale.
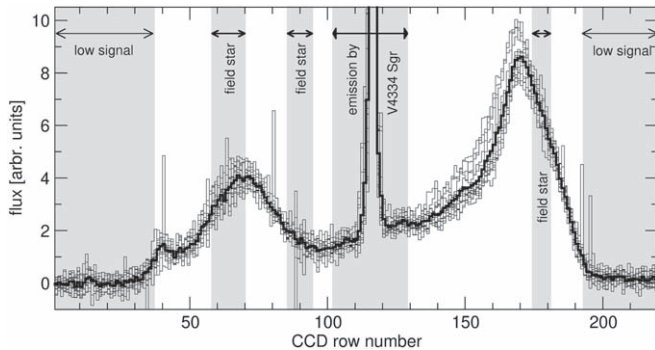

Figure 5. The 16 measurements (thin lines) and the derived mean (thick line) of the [N II] 6584 Å line taken in 2010 with the visual band GRISMs V300 and V600. The shaded areas are the applied rejection masks The data value d_i is derived as the mean of the integrals from the unmasked regions.

fraction of the time series. The [O I] 6300+6363 Å pair was significantly affected by telluric lines, and could not be fully recovered. The partly resolved [S II] 6716+6732 Å pair was summed to improve the signal-to-noise ratio.

The data from different instrumental configurations of the same line show small variations between the different sets but do not show systematic trends. Different instrument setups also show no systematic effects. Up to 20 measurements were available per year. Moreover, the three line pairs, H I 6563+4861 Å, [O III] 4958+5007 Å, and [S III] 9068+9530 Å, are tightly coupled by quantum mechanics and have well determined line ratios. Their consistency provides an additional quality test for the calibration.

4. Results

We analysed the change as a function of time, by using annual groups of line intensities for each instrumental setup as independent data points d_i. The baseline is taken as time $t_0 = 2012.45$, which is the mean time point of our original data, 16.31 years after the discovery of the event (Nakano et al. 1996). The total process follows an exponential decline (see Equation (7)). As the total timescale τ_{rec} is so much longer than the epoch of our investigation, a free parameter, giving the curvature of the exponential, cannot be derived unambiguously and numerically stably. Thus we use the Taylor series linear approximation here. We derive independent model regression points m_i of the type

$$m_i = c\,(t_i - t_0) + n,$$
$$\text{where}\quad \sum_i \frac{(d_i - m_i)^2}{\sigma_i^2} \to \text{Min}, \tag{2}$$

with c being the average annual change. As mentioned above the errors σ_i vary strongly for some lines (see also Table 2). Thus Equation (2) does not resemble the χ^2 definition where $\sigma_i \propto \sqrt{m_i}$ anymore. Thus standard regression algorithms used widely do not apply (York 1966; Giordano & Iavernaro 2021; Lecuna et al. 2020). The regression analysis follows Tellinghuisen (2020). The derived value of n normalizes each of the data sets with respect to the line strengths at t_0. This is slightly different from using just a weighted mean for the time t_0, but is numerically more stable against the strong year-on-year variations of the errors, which are seen especially for the helium lines. For the regression the `mpfit` library

5

Table 2
The Measured Annual Values and the Standard Deviations Normalized to the Epoch $t_0 = 2012.45$: $\bar{d}_i := d_i/n$ and $\bar{\sigma}_i := \sigma_i/n$

Year	He II λ4686		H I λ4861		O III λ4958		O III λ5007		He I λ5875		H I λ6563				N II λ6584			
	$\bar{d}_i^V$	$\bar{\sigma}_i^V$	$\bar{d}_i^V$	$\bar{\sigma}_i^V$	$\bar{d}_i^V$	$\bar{\sigma}_i^V$	$\bar{d}_i^V$	$\bar{\sigma}_i^V$	$\bar{d}_i^V$	$\bar{\sigma}_i^V$	$\bar{d}_i^V$	$\bar{\sigma}_i^V$	$\bar{d}_i^I$	$\bar{\sigma}_i^I$	$\bar{d}_i^V$	$\bar{\sigma}_i^V$	$\bar{d}_i^I$	$\bar{\sigma}_i^I$
2007	0.999	0.436	1.007	0.149	1.018	0.078	1.016	0.060	1.128	0.606	0.979	0.082			0.831	0.070		
2008	1.007	0.564	1.073	0.084	1.158	0.069	1.157	0.074	1.062	0.380	1.125	0.099			0.990	0.073		
2009	0.884	0.538	0.917	0.138	0.946	0.067	1.006	0.238	0.770	0.360	0.894	0.056	1.027	0.117	0.920	0.088	0.818	0.108
2010	1.131	0.879	0.964	0.335	1.058	0.320	1.135	0.381	0.924	0.696	1.031	0.305	1.027	0.070	1.012	0.271	0.924	0.067
2011											0.992	0.070			0.946	0.098		
2012	1.281	0.807	1.055	0.110	0.974	0.101	0.979	0.095	1.410	1.328	0.994	0.080	1.018	0.074	1.017	0.064	1.039	0.123
2013	0.937	0.299	1.102	0.474	0.957	0.101	1.005	0.108	1.833	1.663	1.018	0.085	1.146	0.125	1.203	0.178	1.035	0.184
2014	1.396	1.291	1.197	0.400	1.018	0.104	1.027	0.122	1.391	1.638	1.085	0.098	1.347	0.216	1.446	0.196	1.132	0.106
2015	1.706	1.474	1.005	0.065	0.906	0.105	0.940	0.089	1.626	1.254	0.983	0.067	1.081	0.150	1.163	0.179	1.057	0.063
2016													0.972	0.120			1.070	0.150
2017	0.954	0.815	0.930	0.073	0.862	0.110	0.885	0.066	1.034	0.498	0.904	0.102	0.994	0.158	1.172	0.172	1.092	0.071
2022	1.089	0.500	0.920	0.090	0.765	0.130	0.774	0.070	1.002	0.340	0.950	0.070	0.910	0.100	1.325	0.090	1.250	0.130

Year	S II λ6716+λ6732				Ar III λ7136				S III λ9068		S III λ9560	
	$\bar{d}_i^V$	$\bar{\sigma}_i^V$	$\bar{d}_i^I$	$\bar{\sigma}_i^I$	$\bar{d}_i^V$	$\bar{\sigma}_i^V$	$\bar{d}_i^I$	$\bar{\sigma}_i^I$	$\bar{d}_i^I$	$\bar{\sigma}_i^I$	$\bar{d}_i^I$	$\bar{\sigma}_i^I$
2007	0.994	0.161			0.681	0.429						
2008	1.160	0.229			1.015	0.097	0.941	0.157				
2009	0.959	0.339	0.771	0.224	0.866	0.371	0.940	0.770	0.959	0.107	0.954	0.096
2010	0.865	0.179	0.873	0.098	1.133	0.604	0.950	0.798	0.921	0.087	0.942	0.100
2011			0.932	0.115	0.887	0.272	1.072	0.192	1.044	0.107		
1012	1.015	0.164	1.139	0.276	1.086	0.377	1.381	0.728	1.048	0.081	1.043	0.135
2013	0.994	0.227	1.193	0.276	1.057	0.706	0.825	0.558	1.100	0.165	1.093	0.176
2014	1.526	0.264	1.099	0.199	1.352	0.772	1.486	1.518	1.292	0.261	1.234	0.210
2015	1.249	0.405	1.093	0.230	1.162	0.635	1.219	0.353	1.128	0.205	1.015	0.124
2016	1.193	0.316		1.305	0.902			0.884	0.116	0.955	0.161	
2017	1.128	0.175	1.174	0.555	0.918	0.476	1.162	0.878	1.081	0.309	0.947	0.306
2022	1.273	0.231	1.340	0.250	1.100	0.380	1.196	0.104	1.134	0.114		

Note. The superscript indicates if the values are obtained by the visual (V) band 300V and 600V GRISM or by an infrared (I) band 300I, 600I and 600z GRISM.
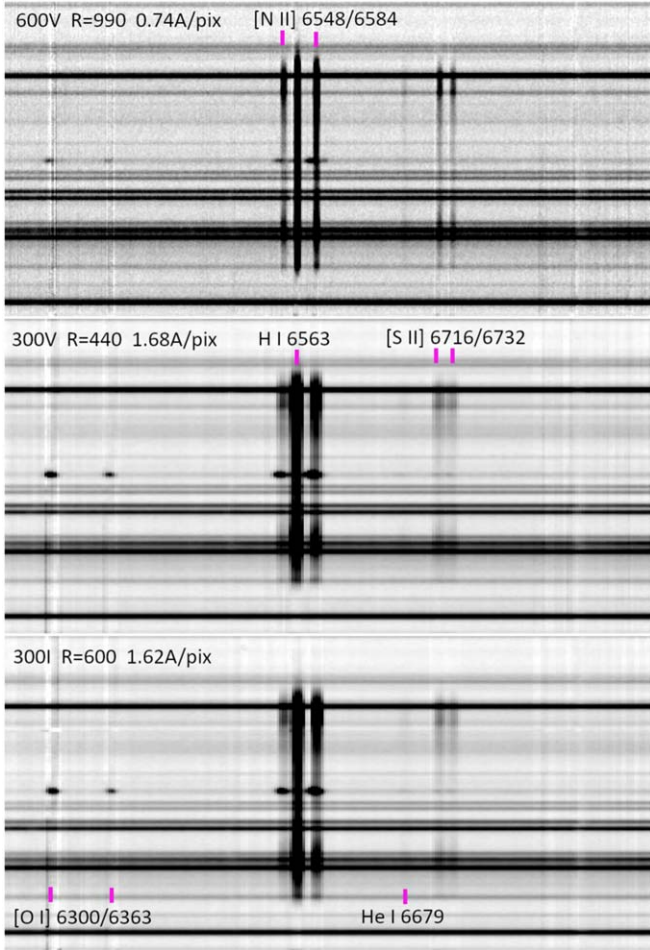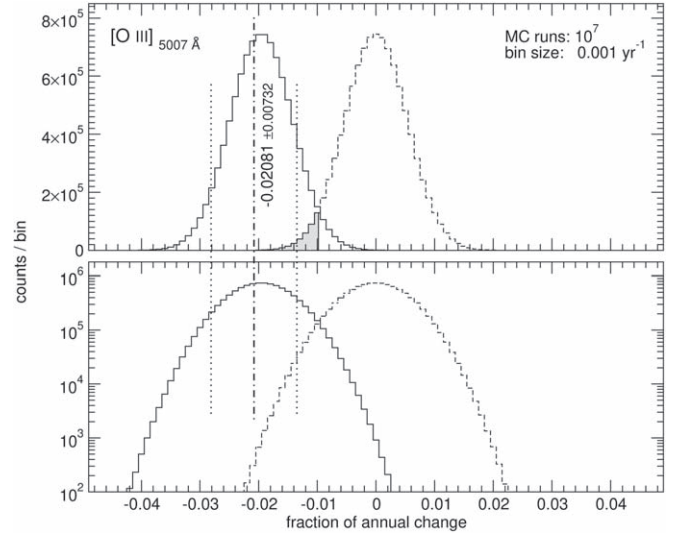
Figure 7. The distribution of the C_k parameter (solid line) and of the constant solution (dashed line) were derived using the MC runs for the [O III] line at 5007 Å. The shaded area gives the parameter A for the determination of x in Equation (5). The fit and the region of the standard error derived from a normal regression program are shown for reference with the dashed–dotted and dotted lines, respectively.

Figure 6. The overlapping region of the 600V (upper), 300V (middle), and 300I (lower) GRISMs from 6250 Å to 6950 Å after sky emission line removal showing the effects of the different resolutions as well as contamination by field stars and the clumpy emission of the central object V4334 Sgr itself.

(Markwardt 2009) was used, with the variable errors handled according to York (1966) in the implementation of Tellinghuisen (2020). The errors given by the mpfit library for the c parameter represent the statistical error with two parameters for the calculation of the degrees of freedom. However, we are primarily interested in the significance of any slope, rather than the parameter c (respectively, its normalized counterpart C_k from Equation (3)) and its potential contribution to the statistical error budget. To derive the significance of the slope, a C program was written to perform a Monte Carlo (MC) simulation. The value n from Equation (2) defines the normalized values $\bar{d}_i := d_i / n$ and $\bar{\sigma}_i := \sigma_i / n$ given in Table 2. Each data point $\bar{d}_i$ was varied independently 10 million times in agreement with its individual Gaussian error distribution, and a new regression for the normalized change $C_k \, \forall \, k \in [1, 10^7]$ was calculated with model points M_i types as

$$M_i = C_k \, (t_i - t_0) + N_i,$$
$$\text{where} \quad \sum_i \frac{(\bar{d}_i - M_i)^2}{\bar{\sigma}_i^2} \to \text{Min.} \tag{3}$$

Moreover, a similar set of parameters from the same MC simulated data points, assuming that there was no change in

time-defining model points M, was derived

$$M_i = N_i,$$
$$\text{where} \quad \sum_i \frac{(\bar{d}_i - M_i)^2}{\bar{\sigma}_i^2} \to \text{Min.} \tag{4}$$

The fractional area of overlap A between the "sloping" and "non-sloping" distribution functions yields the statistical significance $(1 - A)$ of the slope as a single parameter. This significance is lower than what would be derived from the standard deviation of the inclination (relative change per year) given by the fit with two free parameters. Figure 7 shows an example of such a pair of histograms. A priori this solution of the MC simulation, caused by the wide spread of errors between the individual data points, does not have to be distributed as a Gaussian. Tests indeed showed that it deviates from solutions with large slopes. As the result for our cases only shows very small slopes, there is only a marginal deviation from a Gaussian. As the assumption of a regular standard deviation holds we are able to use the error function erf from the integral of the Gaussian according to Equation (5) to derive the size of the intersect

$$A = 1 - \text{erf}\left(-\frac{x}{\sqrt{2}}\right), \tag{5}$$

and from this the level $x \times \sigma$ of significance.

Despite the fact that some lines are coupled by physical and quantum mechanical processes, each line was treated individually in this statistical process. This gives additional confidence about the stability of the analysis. The results are shown in Figure 8, and Table 3 lists the annual changes and the statistical uncertainties compared to a constant solution derived from the MC simulations. The hydrogen and the helium lines show, as expected by most models, no variations with time during our survey. Both [O III] lines show independently the same weak decline in intensity by about 2% per year, while the
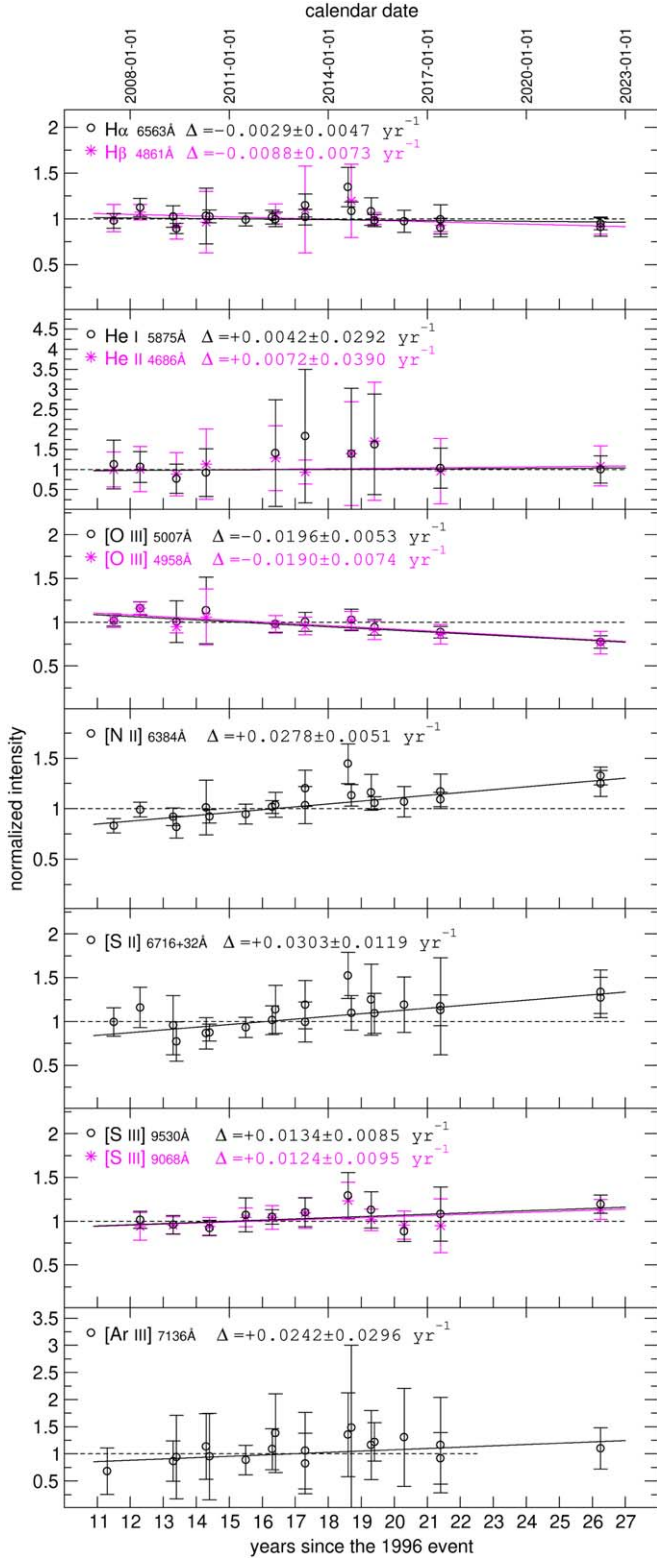
Figure 8. The time evolution of various permitted lines of H I, He I, and He II and the forbidden line transitions of [O III], [N II], [S II], [S III], and [Ar III]. The best linear fits are indicated. The dashed lines indicate the constant solution.

Table 3
The Annual Changes of the Various Lines Together with the Significance x in Terms of σ Relative to an Unchanging Calculation in the MC Simulations

Ion	Wavelength (Å)	A	$x \times \sigma$	Relative Change per Year Δ
H I	6563	0.465	0.73	-0.0029 ± 0.0047
H I	4861	0.325	0.98	-0.0088 ± 0.0072
He I	5875	0.493	0.69	0.0042 ± 0.0292
He II	4686	0.558	0.59	0.0072 ± 0.0390
N II	6584	0.0076	**2.66**	0.0278 ± 0.0051
O III	4958	0.1255	**1.53**	-0.0190 ± 0.0074
O III	5007	0.0447	**2.01**	-0.0196 ± 0.0053
Ar III	7136	0.349	0.94	0.0242 ± 0.0296
S II	6716+32	0.112	**1.59**	0.0303 ± 0.0119
S III	9068	0.283	1.07	0.0124 ± 0.0095
S III	9530	0.260	1.13	0.0134 ± 0.0085

Note. The only solutions with $x > 1.5\sigma$ are in bold.

Table 4
The Fractional Population of Selected Ionization Stages from the CLOUDY Model of Juffinger (2021), in Percentages

Ionization Stage	[II]	[III]	[IV]
Helium	81	18	
Carbon	15	80	4
Nitrogen	27	67	6
Oxygen	26	70	3
Sulfur	18	73	8
Chlorine	14	76	10
Argon	3	90	7

Moreover, the identical behavior of the independently treated pairs of [O III] and of [S III] strengthens the statement of the evolution found.

5. Discussion

The Z^2 dependence of the recombination rate on the charge of an ion (see Equation (1)) causes the observed states of O^{++}, S^{++}, and Ar^{++} to react fastest to the sudden loss of the UV radiation field. As the observed line levels are collisionally excited, the line strength is related to the total population of the species for a constant electron temperature; e.g., the [O III] lines in our spectra originate from the first exited term above the ground state and are mostly collisionally excited. The line intensity of the 5007/4958 Å transitions thus is directly proportional to the amount of O^{++}.

The population of the particular ionization state decreases because of direct recombination losses and increases because of recombination of the higher ionization states (O^{3+}, S^{3+}, and Ar^{3+}). CLOUDY photoionization models of the pre-outburst PN by Pollacco (1999, 2002) and Juffinger (2021) show that O^{3+} was not populated significantly ($\leqslant 3\%$), while S^{3+} and Ar^{3+} had a population of about 8% each. Hence, recombination for the higher levels can be ignored for these three species. However, more detailed estimates follow below.

The fractional population of various ionization stages are listed in Table 4. These are calculated from the CLOUDY model (Juffinger 2021), and averaged over an area to account for the narrow slit used in the observations.

For the radiative recombination factor $\alpha_{RR}(T, Z)$ we used the data from Badnell (2006), while for the dielectric component

low ionized species [N II] and [S II] show a weak strengthening of about 3% per year. The effects are small compared to the errors just at the boundary to be detected and thus support the models predicting a slow evolution (see the discussion below).

$\alpha_{DR}(T, Z)$ the calculation is based on the C-like sequence of Zatsarinny et al. (2004) in the updated web-based version of the group (Badnell 2019). The same data are used for the current version of CLOUDY c17 (Ferland et al. 2017) as well. Following Osterbrock & Ferland (2006) these two components can be simply added together to obtain $\alpha(T, Z)$. The modern values differ slightly from the often used values in the tables of Osterbrock & Ferland (2006), which are based on somewhat older calculations (Verner & Ferland 1996; Mazzotta et al. 1998 and references therein). The older values were used to estimate timescales by Pollacco (1999) and Lechner & Kimeswenger (2004), and lead to a somewhat faster than expected evolution.

The recombination timescale τ_{rec} is then given by

$$\tau_{rec} = \frac{1}{\alpha(Z, T_e) \, n_e}, \qquad (6)$$

with Z the ionic charge, T_e the electron temperature, and n_e the electron density. Diagnostic diagrams of observed spectral line ratios yield $T_e \gtrsim 11{,}000$ K and $140 \leqslant n_e \leqslant 180 \, \text{cm}^{-3}$ (Pollacco 1999; Kerber et al. 1999; Juffinger 2021). These values are typical for old PNe generally (see, e.g., Öttl et al. 2014; Barría et al. 2018). This density is much lower than the one used in the test for dynamical evolution with CLOUDY by van Hoof et al. (2020). We use the upper limit of $n_e \approx 180 \, \text{cm}^{-3}$ for our estimates. Lower values will result in an even slower evolution.

The timescale for the recombination of the small (3%) O^{3+} population becomes only 13 yr. Accounting for this and assuming all O^{3+} was added quickly to O^{++}, this ionization state covers more than 73% of the total amount of oxygen in the CLOUDY models. The predicted timescale of O^{++} recombination is $t \approx 61$ yr, leading to about a 25% decline from the 1996 outburst until the epoch at the end of our observations.

This prediction is within the bounds of the observational result in Table 3. Using an undisturbed and thus exponential decline

$$n_{ion}(t) = n_{ion}(0) \exp\left(-\frac{t}{\tau_{rec}}\right),$$

$$\frac{d}{dt} n_{ion}(t) = -n_{ion}(0) \frac{1}{\tau_{rec}} \exp\left(-\frac{t}{\tau_{rec}}\right), \qquad (7)$$

leads in our observations to a timescale of about 50 yr. Within the uncertainties of the density estimates and the statistical uncertainties this matches well. The rate of decline is about an order of magnitude slower than the values given by Pollacco (1999).

The populations of S^{3+} and Ar^{3+} with timescales of 11 and 16 yr, respectively, would depopulate those states by about 75% each. This adds about 7% to S^{++} and Ar^{++}. The latter states, originally populated by about 73 and 90% of the total sulfur and argon, respectively, have timescales of 40 and 50 yr to recombine to S^+ and Ar^+. Thus even with the compensation by the faster recombining of higher levels, we predict a decline of about 50%. The observations do not confirm a significant decline. Both states show an increase at the 1σ level. Due to the higher errors, the Ar^{++} observations are consistent with the predicted timescale only at the 2σ level (probability $\lesssim 2\%$). For

S^{++}, the discrepancy is in excess of 4.5σ and thus highly significant.

The observed increase of the lines of the low ionization stages N^+ and S^+ reflect their populations of, respectively, 27% and 18% pre-outburst. Their lifetimes are 250 yr or more. Thus even a limited fraction of recombination from the upper ionization states will yield a significant strengthening of the [N II] and [S II] lines.

The recombination timescales calculated for hydrogen H^+ and He^+ are 450 yr or more. This is supported well by the observations, which do not indicate any changes in these emission lines. Moreover, as those elements outnumber the other ions by 2 orders of magnitude, the fraction of the total energy density bound in ionization does not change at all.

The nebular expansion could also affect flux evolution due to decreasing electron density. However, the measured expansion of 30 ± 3 km s^{-1} (Juffinger 2021) leads to an estimated decrease by a factor of 7×10^{-4} per year and unit volume. This is much slower than the expected effect from recombination and below the accuracy of the observations themselves.

6. Sulfur

A notable discrepancy with the predicted evolution is seen for sulfur, where the [S III] lines are constant in strength whereas the models predict a decrease. This can come from an additional source of S^{2+} which balances the recombination.

Measured sulfur abundances in PNe are anomalously low (Henry et al. 2012) compared to other elements. The sulfur deficit is up to a factor of 2. Possible causes are discussed by Henry et al. (2012). They state that in some cases, telluric absorption near [S III] 9068+9530 Å may be present. In our case, the resolution is very good and the very long FORS slits allow excellent sky reduction. However, the sulfur problem is most pronounced for high-ionization, matter-bounded nebulae. This suggests that the models may be missing higher ionization stages, leading to underestimated ionization correction factors. Direct measurements of infrared [S IV] lines have provided support for this conclusion (Henry et al. 2012), as these find a higher than predicted abundance of this ionization stage for these nebulae.

The old PN of Sakurai's star falls in the category of high-excitation, matter-bounded nebulae. If the S^{3+} abundance is higher than predicted in the model, the fast recombination from this level would increase the source function of S^{2+}. Higher ionization stages, S^{4+} and higher, could contribute since they would recombine very fast to S^{3+}.

We recalculated the expected abundance change of S^{2+} for variable abundances of S^{3+} and higher ionization stages. The measured change with 1σ errors can be reproduced if the higher ionization stages account for $65\% \pm 16\%$ of sulfur, as opposed to 10% in the CLOUDY model. This gives a total sulfur abundance that is around 55% higher than in the model, which is within the typical range of the sulfur anomaly.

A sulfuric dust component, which is another explanation for the anomaly, would not affect the recombination rates. More accurate data will be needed for this analysis, but the apparent recombination discrepancy suggests that higher ionization stages may be involved in part or all of the observed sulfur anomaly.

Reichel et al.

7. Conclusions

We were able for the first time to follow the recombination evolution of a very low-density galactic gaseous nebula. A careful analysis determined the order of magnitude of the effects of recombination. This result excludes by orders of magnitudes some faster evolutionary scenarios postulated before. While oxygen seems to follow the predicted evolution for updated atomic data, other metals do not agree as well, and especially sulfur deviates significantly from the predictions.

For sulfur, the lack of fading of the [S IV] lines points to possible recombination from unobserved higher ionization levels. There is some evidence that the sulfur anomaly (e.g., sulfur abundance deficit) may be caused by unexpectedly high levels of S^{4+}. The current investigation has led to some support for this. Other explanations have also been proposed and it is important to continue these studies.

The high efficiency of energy transfer by fluorescence calculated by Deguchi (1985) suggests that this increases the ionization levels of the metals. Electron transfer reactions from long-lived ionized hydrogen and helium may also add to this. As those long-living species outnumber the metals by orders of magnitudes, their excitation energies and electron losses could affect the metals without significantly changing their own abundances. The theoretical recombination rates may therefore be subject to change.

In conclusion, these observational results can be useful for validating more complex time-evolution models (see, e.g., van Hoof et al. 2020 and references therein) which are in development. The simplified recombination timescale calculated previously (Pollacco 1999; Lechner & Kimeswenger 2004; Balick et al. 2021) may have to be revisited, while the estimates of an even much faster evolution by Schönberner (2008), assuming timescales well below a year, are not confirmed. Further monitoring of V4334 Sgr will be needed to improve the significance of the results, but the results are encouraging and unique.

ORCID iDs

Martin Reichel ● https://orcid.org/0000-0002-1365-9336
Stefan Kimeswenger ● https://orcid.org/0000-0003-2379-0474
Peter A. M. van Hoof ● https://orcid.org/0000-0001-7490-0739
Albert A. Zijlstra ● https://orcid.org/0000-0002-3171-5469
Daniela Barría ● https://orcid.org/0000-0003-4754-4673
Marcin Hajduk ● https://orcid.org/0000-0001-6028-9932
Griet C. Van de Steene ● https://orcid.org/0000-0001-7628-7499
Daniel Tafoya ● https://orcid.org/0000-0002-2149-2660

References

Anderson, J., Mieske, S., & Kaufer, A. 2017, Very Large Telescope Paranal Science Operations FORS2 User Manual (101st ed.; Garching: European Southern Observatory)
Appenzeller, I., Fricke, K., Fürtig, W., et al. 1998, Msngr, 94, 1
Arkhipova, V. P., Esipov, V. F., & Ikonnikova, N. P. 2009, AstL, 35, 633
Badnell, N. R. 2006, ApJS, 167, 334
Badnell, N. R. 2019, Fits for Total Dielectronic Recombination Rate Coefficients, http://amdpp.phys.strath.ac.uk/tamoc/DATA/DR/clist_eV
Balick, B., Guerrero, M. A., & Ramos-Larios, G. 2021, ApJ, 907, 104
Banse, K., Crane, P., Grosbol, P., et al. 1983, Msngr, 31, 26
Barría, D., Kimeswenger, S., Kausch, W., & Goldman, D. S. 2018, A&A, 620, A84
Bublitz, J., Kastner, J. H., Hily-Blant, P., et al. 2022, A&A, 659, A197
Clayton, G. C., Sugerman, B. E. K., Stanford, S. A., et al. 2011, ApJ, 743, 44
Deguchi, S. 1985, ApJ, 291, 492
Ducati, J. R., Bevilacqua, C. M., Rembold, S. B., & Ribeiro, D. 2001, ApJ, 558, 309
European Southern Observatory 2013, ESO-MIDAS: General tools for image processing and data reduction, Astrophysics Source Code Library, ascl:1302.017
Ferland, G. J., Chatzikos, M., Guzmán, F., et al. 2017, RMxAA, 53, 385
Giordano, D., & Iavernaro, F. 2021, Math. Meth. Appl. Sci., 44, 6448
Hajduk, M., Todt, H., Hamann, W.-R., et al. 2020, MNRAS, 498, 1205
Hajduk, M., Zijlstra, A. A., Herwig, F., et al. 2005, Sci, 308, 231
Henry, R. B. C., Speck, A., Karakas, A. I., Ferland, G. J., & Maguire, M. 2012, ApJ, 749, 61
Herwig, F. 2001, ApJL, 554, L71
Hinkle, K. H., & Joyce, R. R. 2014, ApJ, 785, 146
Hinkle, K. H., Joyce, R. R., Matheson, T., Lacy, J. H., & Richter, M. J. 2020, ApJ, 904, 34
Jones, A., Noll, S., Kausch, W., et al. 2019, A&A, 624, A39
Jones, A., Noll, S., Kausch, W., Szyszka, C., & Kimeswenger, S. 2013, A&A, 560, A91
Juffinger, I. 2021, Master's thesis, Leopold-Franzens Universität Innsbruck, https://resolver.obvsg.at/urn:nbn:at:at-ubi:1-97911
Kerber, F., Köppen, J., Roth, M., & Trager, S. C. 1999, A&A, 344, L79
Kimeswenger, S., Thorstensen, J. R., Fesen, R. A., et al. 2021, A&A, 656, A145
Koller, J., & Kimeswenger, S. 2001, ApJ, 559, 419
Koskela, A., Dalnodar, S., Kissmann, R., et al. 2012, in IAU Symp. 283, Planetary Nebulae: An Eye to the Future, ed. A. Manchado et al. (Cambridge: Cambridge Univ. Press), 412
Kreckel, H., Novotný, O., & Wolf, A. 2019, RSPTA, 377, 20180412
Lawlor, T. M. 2021, MNRAS, 504, 667
Lawlor, T. M., & MacDonald, J. 2003, ApJ, 583, 913
Lechner, M. F. M., & Kimeswenger, S. 2004, A&A, 426, 145
Lecuna, M., Pennecchi, F., Malengo, A., & Spazzini, P. G. 2020, MeScT, 31, 114004
Markwardt, C. B. 2009, in ASP Conf. Ser. 411, Astronomical Data Analysis Software and Systems XVIII, ed. D. A. Bohlender, D. Durand, & P. Dowler (San Francisco, CA: ASP), 251
Mazzotta, P., Mazzitelli, G., Colafrancesco, S., & Vittorio, N. 1998, A&AS, 133, 403
Miller Bertolami, M. M., Althaus, L. G., Serenelli, A. M., & Panei, J. A. 2006, A&A, 449, 313
Mitrofanova, A. A., Shimansky, V. V., Borisov, N. V., Spiridonova, O. I., & Gabdeev, M. M. 2016, ARep, 60, 252
Moehler, S., García-Dabló, C. E. S., Freudling, W., & Sterzik, M. 2019, FORS2 Spectroscopy Reflex Tutorial and Cookbook (1st ed.; Garching: European Southern Observatory)
Nakano, S., Sakurai, Y., Hazen, M., et al. 1996, IAU Circ., 6322, 1
Osterbrock, D. E., & Ferland, G. J. 2006, Astrophysics of Gaseous Nebulae and Active Galactic Nuclei (2nd ed.; Sausalito, CA: Univ. Science Books)
Osterbrock, D. E., Fulbright, J. P., Martel, A. R., et al. 1996, PASP, 108, 277
Öttl, S., Kimeswenger, S., & Zijlstra, A. A. 2014, A&A, 565, A87
Patat, F., Moehler, S., O'Brien, K., et al. 2011, A&A, 527, A91
Pavlenko, Y. V., & Duerbeck, H. W. 2001, A&A, 367, 933
Pollacco, D. 1999, MNRAS, 304, 127
Pollacco, D. 2002, Ap&SS, 279, 129
Reichel, M. 2021, Master's thesis, Leopold-Franzens Universität Innsbruck, https://resolver.obvsg.at/urn:nbn:at:at-ubi:1-91521
Reindl, N., Rauch, T., Miller Bertolami, M. M., Todt, H., & Werner, K. 2017, MNRAS, 464, L51
Schönberner, D. 2008, in ASP Conf. Ser. 391, Hydrogen-Deficient Stars, ed. A. Werner & T. Rauch (San Francisco, CA: ASP), 139

Tachiev, G., & Froese Fischer, C. 2001, CaJPh, 79, 955

Tellinghuisen, J. 2020, AnaCh, 92, 10863

Tylenda, R. 1980, AcA, 30, 433

Van de Steene, G. C., van Hoof, P. A. M., Kimeswenger, S., et al. 2017, in IAU Symp. 323, Planetary Nebulae: Multi-Wavelength Probes of Stellar and Galactic Evolution, ed. X. Liu, L. Stanghellini, & A. Karakas (Cambridge: Cambridge Univ. Press), 380

van Hoof, P. A. M., Hajduk, M., Zijlstra, A. A., et al. 2007, A&A, 471, L9

van Hoof, P. A. M., Kimeswenger, S., Van de Steene, G., et al. 2018, Galax, 6, 79

van Hoof, P. A. M., Van de Steene, G. C., Beintema, D. A., et al. 2000, ApJ, 532, 384

van Hoof, P. A. M., Van de Steene, G. C., Guzmán, F., et al. 2020, CoSka, 50, 32

Verner, D. A., & Ferland, G. J. 1996, ApJS, 103, 467

Warmels, R. H. 1992, in ASP Conf. Ser. 25, Astronomical Data Analysis Software and Systems I, ed. D. M. Worrall, C. Biemesderfer, & J. Barnes, 115

York, D. 1966, CaJPh, 44, 1079

Zatsarinny, O., Gorczyca, T. W., Korista, K. T., Badnell, N. R., & Savin, D. W. 2004, A&A, 417, 1173